Predicting the resistivity signature of internal erosion in freshwater embankment dams: anomaly polarity, detectability, and a full-scale benchmark

Seokhoon Oh[1,*]

[1] Department of Energy and Resources Engineering, Kangwon National University, 1 Gangwondaehak-gil, Chuncheon, Gangwon 24341, Republic of Korea

[*] Corresponding author: gimul@kangwon.ac.kr

Peer-review status

This manuscript is a **non-peer-reviewed preprint** submitted to **EarthArXiv**. It has not been peer reviewed. A version of this manuscript is being prepared for submission to a peer-reviewed journal; this coversheet will be updated upon submission.

Data and code availability

All scripts and result files reproducing every figure and table are openly archived on Zenodo: `https://doi.org/10.5281/zenodo.20658789`

July 2026

Predicting the resistivity signature of internal erosion in freshwater embankment dams: anomaly polarity, detectability, and a full-scale benchmark

Seokhoon Oh

[a] *Department of Energy and Resources Engineering, Kangwon National University, 1 Gangwondaehak-gil, Chuncheon, 24341, Gangwon, Republic of Korea*

Abstract

Electrical resistivity tomography (ERT) is a standard tool for embankment-dam inspection, and low-resistivity anomalies are conventionally read as leakage or internal erosion. High-resistivity signatures of internal erosion have been reported repeatedly but never derived from petrophysical first principles. We show why: for the freshwater reservoirs and clayey cores of most inland dams, about 97 % of intact-core conduction is clay surface conduction, so erosion that removes fines and replaces them with fresh water *raises* resistivity, and a closed-form criterion, $\sigma_w(F^* - 1) > B\,Q_v$, places typical inland reservoirs a factor of 3–10 inside the resistive-damage regime — explaining, and reconciling, the contradictory anomaly polarities reported in the literature. For a reference crest-survey geometry, defect signals follow $A_{\max} \approx 45(D/z)^2$; combined with a voltage-dependent, site-calibratable error model and geostatistical background variability, this implies that pipe-class defects ($\leq$3 m) are not reliably detectable in single-epoch data, while conventional anomaly thresholds can generate spurious indications in defect-free ground; degraded reaches ($\geq$5–10 m) are resolved by a single survey or time-lapse — the latter also suppressing false positives — whereas pipe-class defects need active contrast or complementary methods. A reconstruction of the published Älvkarleby full-scale test embankment from published inputs alone reproduces the observed anomaly polarity for

Email address: gimul@kangwon.ac.kr (Seokhoon Oh)

all six engineered defects, the detection ranking, and the necessity of multi-year averaging. We provide the phase diagram, detectability charts, a reciprocal-measurement site-calibration procedure and an openly archived workflow that allow the expected polarity and the detection limit of a planned survey to be computed before it is commissioned. The results suggest that, in freshwater clay-core dams, low-resistivity anomalies should generally be read as possible downstream consequences of leakage — wetting or fines redeposition — rather than as direct images of core damage.

Keywords: embankment dam, internal erosion, electrical resistivity tomography, detectability, Waxman–Smits, survey design

---

1. Introduction

Internal erosion is among the leading causes of embankment-dam failure, and its early manifestations — concentrated leaks, suffusion of core fines, contact erosion — are notoriously difficult to observe from the surface. Electrical resistivity tomography (ERT) has therefore become a standard component of dam safety investigations worldwide (e.g., Cho and Yeom, 2007; Sjödahl et al., 2008), attractive because it is non-invasive, sensitive to water content and soil texture, and deployable along the crest of an operating dam. In routine practice, the interpretation rule applied to the resulting sections is almost universal: zones of *anomalously low resistivity* are flagged as suspected leakage paths or damaged core. The intuition behind the rule — more water means higher conductivity — is rarely questioned.

This paper shows, and quantifies, why for the most common configuration of inland dams the rule is physically inverted. A compacted clayey core is itself an excellent electrical conductor, not because of its pore water but because of surface conduction in the electrical double layer of the clay minerals. Fresh reservoir water is, by comparison, a poor conductor. When internal erosion removes core fines and the resulting void or coarsened zone is occupied by fresh water (or by washed-in filter sand), the process replaces a conductor with an

insulator: the damaged zone should appear *resistive*, not conductive. Pieces of evidence for this inverted polarity are scattered through the literature. Sjödahl et al. (2008), monitoring the Hällby dam, noted that internal erosion may increase resistivity through porosity growth and chose seasonal-variation amplitude rather than absolute resistivity as their diagnostic; laboratory suffusion experiments report order-of-magnitude resistivity increases upon washout of fines (Masi et al., 2020); and at the Älvkarleby full-scale test dam, every internal defect and every later-confirmed zone of real internal erosion expressed itself as a *high*-resistivity, low-chargeability anomaly (Norooz, 2025; Norooz and Dahlin, 2025). The author's own earlier studies raised this caveat in qualitative form: Oh and Sun (2008) observed that an internally eroded core may exhibit *higher* resistivity than the intact clay, and Lee et al. (2020) explicitly distinguished the expected polarity by location — conductive on the wetted downstream shell, potentially resistive within the core. What has been missing is what a practitioner needs: a quantitative criterion stating *under which conditions* the polarity flips, and what the conventional rule's domain of validity actually is.

The interpretation question is inseparable from a second, equally practical one: detectability. Dam owners repeatedly commission crest ERT surveys on structures with independently confirmed defects and receive sections in which "nothing shows". The geophysical literature offers fragments here as well — synthetic studies of dam geometry effects (Sjödahl et al., 2006; Oh, 2012), predesign modelling of a specific test dam (Norooz et al., 2021), array-resolution comparisons on generic targets (Dahlin and Zhou, 2004), and resolution-matrix-based survey optimization (Stummer et al., 2004; Wilkinson et al., 2006, 2012) — but no general, target-explicit answer to "what is the minimum defect this survey can see, with this instrument, at this site?". Without such an answer, a negative survey is uninterpretable: it may mean an intact dam, or a defect below an undisclosed detection limit, or a defect of the opposite anomaly sign to the one being sought.

Here we treat the two questions as one problem with three layers. **(i) Polarity.** Starting from Waxman–Smits petrophysics we derive a closed-form

crossover criterion separating the "damage = conductive" from the "damage = resistive" regime in the plane of pore-water conductivity versus core cation-exchange capacity, and we quantify, by Monte-Carlo propagation of parameter uncertainty, the probability of each anomaly sign for the principal damage modes (open piping channels, suffusion at varying degrees, fines redeposition, downstream wetting). **(ii) Signal.** Using finite-element forward modelling we reduce the data-space signature of a core pipe to a scaling law in defect diameter and depth, quantify the intrinsic detection asymmetry between resistive and conductive targets of equal geometric contrast, and rank the confounding signals (reservoir-level change, seasonal water-quality change, 3-D geometry artefacts) that share the measurement with the defect. **(iii) Decision.** We embed the signal in a voltage-dependent field error model, $e = p + U_f/U$, calibrated and validated by reciprocal measurements, and define a per-datum detection index whose threshold behaviour we test against geostatistically heterogeneous backgrounds and, finally, against the published outcome of the Älvkarleby test embankment — a full-scale structure with six engineered defects whose positions were unknown to the monitoring team.

The objectives of this study are therefore threefold: (1) to derive a petrophysical criterion — and its phase diagram — for the polarity of internal-erosion anomalies in clay-core embankments; (2) to quantify the data-space and inversion-space detectability of pipe- and zone-type defects under realistic, voltage-dependent field errors and geostatistical background variability; and (3) to test the resulting framework against the independently published outcome of the Älvkarleby full-scale test embankment. Two supporting analyses — a reciprocal-measurement calibration of the error model and a heterogeneity Monte Carlo — connect these two pillars to survey-level decisions, and the paper closes with a pre-survey assessment protocol and a reporting checklist for routine practice.

2. Methods

2.1. Petrophysical model and damage scenarios

Bulk conductivity of the clayey core is described by the Waxman–Smits model (Waxman and Smits, 1968),

$$\sigma_b = \frac{\sigma_w + B\,Q_v}{F^*}, \qquad F^* = \varphi^{-m} \tag{1}$$

with the equivalent counter-ion conductance $B(\sigma_w) = 4.6[1{-}0.6\exp(-\sigma_w/1.3)]$ (S m^{-1} per meq cm^{-3}) and the cation-exchange capacity per unit pore volume $Q_v = \rho_g\,\mathrm{CEC}\,(1{-}\varphi)/\varphi$. We emphasize the intended scope of Eq. (1): Waxman–Smits was developed for shaly sands, and it is used here as a first-order, effective description of surface conduction — sufficient to bound anomaly polarity and contrast, not to resolve the full electrochemistry of compacted clays; pore-scale formulations (e.g., Revil-type models) refine, but do not alter, the qualitative structure exploited here. Units are made explicit for reproducibility: for the base case, CEC = 8 meq/100 g = 0.08 meq g^{-1} gives $Q_v = \rho_g\,\mathrm{CEC}\,(1-\varphi)/\varphi = 2.70 \times 0.08 \times 0.65/0.35 = 0.40$ meq cm^{-3}. Granular materials (filters, shells, eroded infill) follow Archie (1942), $\sigma_b = \sigma_w\,\varphi^m S^n$. The base case represents an inland zoned dam: reservoir water 200 μS cm^{-1} ($\rho_w = 50\ \Omega\cdot$m, i.e. $\sigma_w = 0.02$ S m^{-1}, the unit in which σ_w and B·Q_v enter Eq. (1)), compacted CL core with $\varphi = 0.35$, m = 2.0, CEC = 8 meq/100 g, giving an intact-core resistivity of 10.5 $\Omega\cdot$m of which 97 % is carried by the B·Q_v term. Damage end-members are modelled as material replacements: water-filled pipe ($\rho = \rho_w$), sand-filled pipe (Archie, $\varphi = 0.40$), partial suffusion by an explicit mass-balance model: with fines mass fraction f_f (carrying essentially all of the CEC) and an eroded fraction e of those fines, the remaining solid mass is

$$m_s = 1 - e\,f_f \tag{2}$$

the bulk exchange capacity and porosity become

$$\mathrm{CEC}' = \frac{(1-e)\, f_f\, \mathrm{CEC}_f + (1-f_f)\, \mathrm{CEC}_c}{m_s}, \qquad \varphi' = \varphi_{\mathrm{open}} - c\,(\varphi_{\mathrm{open}} - \varphi_0), \qquad \varphi_{\mathrm{open}} = 1 - (1-\varphi_0)\, m_s \tag{3}$$

with a skeleton-collapse factor c ∈ [0,1] spanning open-framework to fully re-consolidated states, and the cementation exponent relaxes toward its clean-granular value as texture coarsens,

$$m' = 1.5 + (m_0 - 1.5)\,(f_f'/f_f) \tag{4}$$

where $f_f' = f_f(1-\mathrm{e})/m_s$ is the residual fines fraction. This suffusion description is phenomenological: it interpolates bulk properties between measured clean-clay and clean-granular end-members rather than resolving pore-scale evolution, and serves only to place the suffusion members on the polarity diagram. Fines redeposition is modelled as the inverse perturbation (CEC ×1.2–1.8, φ ×0.88–0.97), and — as the control where the conventional rule is correct — saturation increase in an initially unsaturated shell. The crossover criterion follows directly from Eq. (1): a water-filled defect appears conductive if and only if

$$\sigma_w\,(F^* - 1) > B(\sigma_w)\, Q_v \tag{1a}$$

Parameter uncertainty is propagated by Monte Carlo ($\mathrm{N} = 2 \times 10^5$) over the documented ranges of Table 1.

Table 1. Petrophysical parameters: base case and Monte-Carlo ranges. The ranges are screening-level priors for low-plasticity clay cores, not site-specific distributions; site-specific EC, CEC and porosity should replace them whenever available.

Parameter	Base case	MC range	Basis
Reservoir water EC, σ_w	200 μS cm^{-1}	50–500	inland monitoring networks; site EC mandatory
Core porosity, φ	0.35	0.30–0.42	compaction records (e $\approx$ 0.54)
Cementation exponent, m	2.0	1.8–2.3	compacted clayey fill
Core CEC	8 meq/100 g	3–25	low-plasticity CL; laboratory CEC preferred
Fines content (<75 μm)	60 %	45–80 %	core specifications
Pore-water concentration factor	1.0	1–2	ion exchange in compacted clay
Grain density, ρ_g	2.70 g cm^{-3}	fixed	—

2.2. Forward and inverse modelling

All numerical experiments use pyGIMLi (Rücker et al., 2017). The reference geometry is a 15-m zoned embankment surveyed by 48 crest electrodes at 2 m spacing. Defect signals are computed as *paired* simulations — defect and reference resistivity assigned on the identical mesh — so that discretization error cancels in the data-space ratio $\Delta \ln \rho_a$; mesh-pair reciprocity checks confirm residual numerical noise $\leq$0.01 %. Pipe-type defects (diameter 0.5–3 m, depths 5–12 m) are swept in 2.5-D; zone-type degradation (panels of width 2–10 m) and all confounder experiments use either 2.5-D or full 3-D prism meshes (up to 2.5×10^5 cells) that include the reservoir wedge, dam slopes and,

for the benchmark, the as-built test-dam geometry. The 2.5-D model space spans ±107 m laterally and 45 m vertically (90 m for the deep variant), with mixed boundary conditions on the far edges, a free surface, and a refinement node 0.1 m beneath every electrode; the 3-D prism domains extend to ±120 m across-dam and 200 m along-dam. Because every defect signal is evaluated as a same-mesh ratio, the headline quantities are insensitive to residual discretization error, which the homogeneous-half-space check bounds at ~0.1 %. Inversions use standard smoothness-constrained Gauss–Newton ($\lambda = 15$, $\chi^2 \approx 1$) to quantify model-space contrast recovery, $\mathrm{CRR} = \Delta \log \rho_{\mathrm{inv}} / \Delta \log \rho_{\mathrm{true}}$. Seasonal time-lapse responses are evaluated as double differences on the 3-D mesh — the defect-present seasonal change minus the defect-free one — which isolates the local fingerprint from the basin-scale seasonal response (Section~3.5).

2.3. Field error model, detection index, and site calibration

Each datum's relative standard error is modelled as $e_i = p + U_f/U_i$, where $U_i = I\rho_{a,i}/|k_i|$ is the measured voltage, p the multiplicative floor and U_f the additive voltage floor; time-lapse modes replace p by the repeatability and carry a $\sqrt{2}$ factor (LaBrecque and Yang, 2001). The detection index $\mathrm{DI}_i = |\Delta \ln \rho_{a,i}|/e_i$ declares a target detectable when max DI > 2 with $\geq$5 qualifying data. The factor of two is the conventional single-reading signal-to-noise floor, and the $\geq$5-datum requirement guards both against isolated outliers and against the reduced effective degrees of freedom that spatially correlated instrument and geological noise impose on nominally independent measurements. Defaults (p = 3 % single survey, 1 %/0.5 % standard/precision monitoring; U_f = 100/20 μV; I = 0.5 A) are conservative literature values, but the framework treats them as *measurements*: we show that fitting binned reciprocal differences (Tso et al., 2017) with $\sigma(R) = p|R| + U_f/I$ recovers planted error parameters with p biased low by 4–9 % and U_f to within ±5 % under 2 % gross-outlier contamination (Monte Carlo, N = 200), and that the resulting DI nonetheless reproduces true detect/non-detect verdicts within ±13 %. The multiplicative term p comes out slightly low because the inverse-variance weighting down-weights the high-

resistance bins that fix its slope, a mildly optimistic direction for DI.

2.4. Heterogeneity Monte Carlo

Background heterogeneity is modelled as a multiplicative log-normal field (standard deviation s = 0.2–0.35 in ln ρ; isotropic Gaussian correlation length L = 5–15 m) generated spectrally and sampled at cell centres. Two questions are separated: the stability of the *paired* (time-lapse) defect signal across field realizations, and the *unpaired* realization-to-realization scatter of ρ_a, which acts as the effective model-error floor — and false-positive generator — for single-survey anomaly hunting against an assumed layered reference.

2.5. Benchmark protocol

The Älvkarleby test embankment (20 × 16 × 4 m, concrete basin; core 21 $\Omega \cdot$ m, reservoir 240 $\Omega \cdot$ m; six engineered defects of 0.05–1.4 m scale; 224 buried electrodes; daily monitoring with reciprocal errors <1 %) is reconstructed exclusively from published values (Norooz et al., 2021, 2024). Our pipeline predicts, per defect, the anomaly sign and DI under two error scenarios (single acquisition, 1 %; long-term temporal average, 0.25 %), and the predictions are compared with the reported field outcomes; no field data are used as model input. The exercise is therefore an out-of-sample consistency check — the model is fixed by independently published material properties and geometry, not tuned to the reported detections — rather than a pre-registered blind prediction.

3. Results

3.1. Anomaly polarity: damage is resistive in fresh water

Table 2 summarizes the base case. The intact core conducts at 10.5 $\Omega \cdot$ m, but only 3 % of that conduction is electrolytic; the remaining 97 % flows through the clay's electrical double layer (the B·Q_v term of Eq. 1). This base-case fraction shifts with CEC, porosity, and pore-water conductivity but stays surface-dominated across Table 1's range. This single number reframes the

interpretation problem: any damage process that removes clay removes the conductor, regardless of how much water takes its place. An open pipe filled with reservoir water (50 $\Omega \cdot$m) raises local resistivity by a factor of 4.7; a pipe infilled with washed-in filter sand reaches 198 $\Omega \cdot$m ($\times$18.8). Progressive suffusion is initially almost silent — removing 30 % of the fines changes bulk resistivity by only +1 %, because the loss of surface conduction is nearly offset by the gain in connected porosity — and then turns measurably resistive (+9 % at 50 % fines loss, +60 % at 80 %). A water-filled hydraulic fracture at 2 % volume fraction changes the bulk by +2 %: invisible. The only conductive responses in the entire damage family are the two processes that *add* fines or water where they were not: redeposition of eroded fines at the filter ($\times$0.70) and — the control case — wetting of an initially unsaturated shell ($\times$0.18, i.e. a five-fold conductivity increase). The conventional rule is thus not wrong physics; it is the physics of the *consequences* of leakage in the downstream shell, misattributed to the damage itself in the core.

Table 2. Damage end-members at the base case, and Monte-Carlo statistics over the ranges of Table 1.

Damage end-member	ρ [$\Omega \cdot$m]	vs. intact	P(ρ increase)	Median ratio
Intact core (reference)	10.5	—	—	—
Piping channel, reservoir water	50.0	$\times$4.7	99.4 %	$\times$6.3
Channel infilled with sand	197.6	$\times$18.8	100 %	$\times$24
Suffusion, 30 % fines loss	10.6	$\times$1.01	—	—

Damage end-member	ρ [$\Omega \cdot$ m]	vs. intact	P(ρ increase)	Median ratio
Suffusion, 50 % fines loss	11.5	×1.09	82.1 %*	×1.10*
Suffusion, 80 % fines loss	16.9	×1.60	—	—
Water-filled fracture (2 vol %)	10.7	×1.02	99.4 %	×1.01
Fines redeposition (filter)	7.4	×0.70	0 %	×0.71
Shell wetting S 0.40→0.95 (control)	337 (from 1902)	×0.18	0 %	×0.22

* pooled over fines loss 20–80 %.

Figure 1 plots intact-core and defect-infill resistivity against water conductivity for cores of CEC 3–25 meq/100 g, marking the crossover salinity; Figure 2 generalizes the base case to the (σ_w, CEC) plane. The crossover criterion $\sigma_w(F^* - 1) > B\,Q_v$ admits a closed-form low-salinity limit $\sigma_w^* \approx 1.84\,Q_v/(F^* - 1)$; solving it exactly places the boundary at 404 μS cm^{-1} for a lean, low-CEC core (3 meq/100 g) and at 1,163–4,680 μS cm^{-1} for typical clay cores (8–25 meq/100 g). Sand-filled defects require 3,500–54,000 μS cm^{-1} to appear conductive. Because this boundary depends on the surface-conductance term, we tested its sensitivity to the Waxman–Smits coefficient: scaling B (equivalently Q_v) by ±50 % moves the CEC = 8 crossover only between 547 and 1,854 μS cm^{-1}, so a typical clay core stays well inside the resistive-damage regime under substantial petrophysical uncertainty. Only a lean, low-CEC core (3 meq/100 g) combined with a 50 % underestimate of B lowers the crossover to

~200 μS cm^{-1} — into the range of more mineralized inland reservoirs, the same boundary regime flagged at HyeonNam (Section~4.1). Within roughly a factor of two of the computed crossover the polarity should be read as indeterminate, to be resolved only with site-measured CEC and pore-water EC rather than from the nominal boundary alone. Inland reservoirs — 100–400 μS cm^{-1} in the Korean monitoring network, a few tens of μS cm^{-1} in Scandinavian impoundments — sit a factor of 3 to 10 *below* the boundary (Fig. 2): deep inside the regime where damage is resistive. Estuarine barriers, tailings facilities and contaminated impoundments sit above it, which is precisely where the conventional rule's success stories cluster.

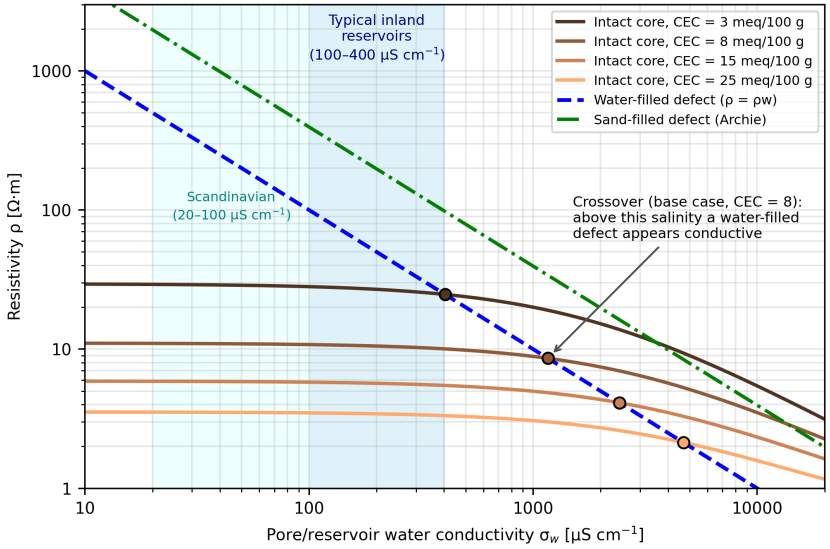

Figure 1: Resistivity of the intact clay core (Waxman–Smits, $\varphi = 0.35$, m = 2.0; curves for CEC = 3–25 meq/100 g) compared with the two damage in-fill end-members — reservoir water (dashed) and clean sand saturated with the same water (dash-dot) — as a function of water conductivity σ_w. Circles mark the crossover salinity at which a water-filled defect stops being resistive relative to the intact core. Shaded bands: typical inland reservoirs (100–400 μS cm^{-1}) and Scandinavian impoundments (20–100 μS cm^{-1}). Saturated conditions, 25 °C.

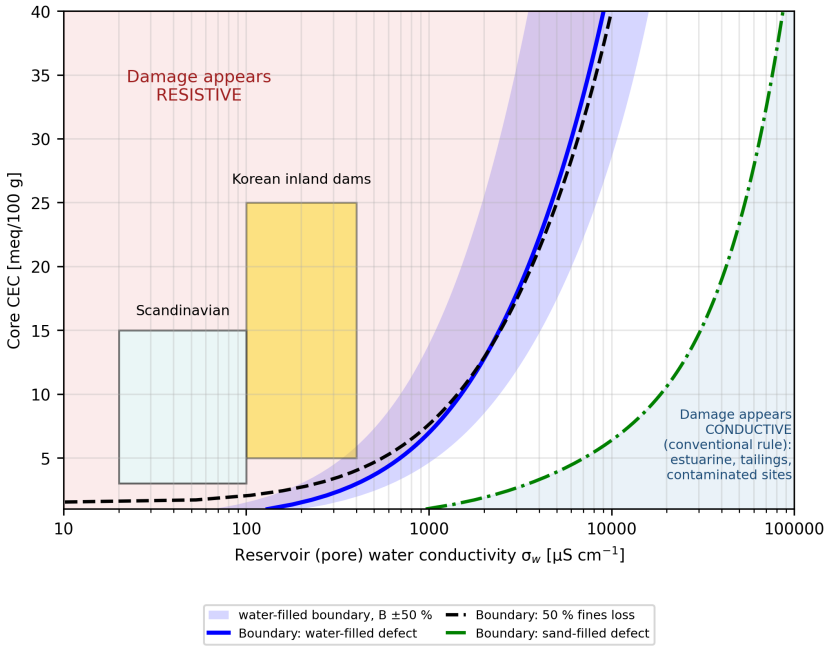

Figure 2: Polarity phase diagram in the (σ_w, CEC) plane for $\varphi = 0.35$, m = 2.0. Curves: crossover boundaries for a water-filled defect (solid), 50 % suffusion (dashed) and a sand-filled defect (dash-dot); left of a boundary the corresponding damage type appears resistive. The shaded band on the water-filled boundary spans a ±50 % change in the Waxman–Smits surface-conductance coefficient B (equivalently Q_v); the Korean and Scandinavian ranges remain in the resistive regime across the band. Boxes: parameter ranges of Korean inland dams and Scandinavian test/monitoring sites — both deep inside the resistive-damage regime; estuarine, tailings and contaminated sites plot to the right, where the conventional "low resistivity = leak" rule is valid. Box provenance: Korean ranges compiled from national water-quality monitoring data and the author's dam investigations [6, 7]; Scandinavian ranges from reported site values at Hällby and Älvkarleby [2, 10].

Monte-Carlo propagation over the full parameter ranges (Fig. 3) shows the conclusion is robust, not an artefact of the base case: the probability that a water-filled pipe raises resistivity is 99.4 % (median ×6.3), a sand-filled pipe 100 % (×24), partial suffusion 82 % (median ×1.10, i.e. mostly weak), and the probability that any core-damage end-member produces a *detectably conductive* anomaly (×0.77 or lower) is ≈0 % within the parameter space of Table 1. The redeposition halo and shell wetting remain reliably conductive (medians ×0.71 and ×0.22), preserving their diagnostic value — as indicators of where leakage water goes, not of where the core is damaged.

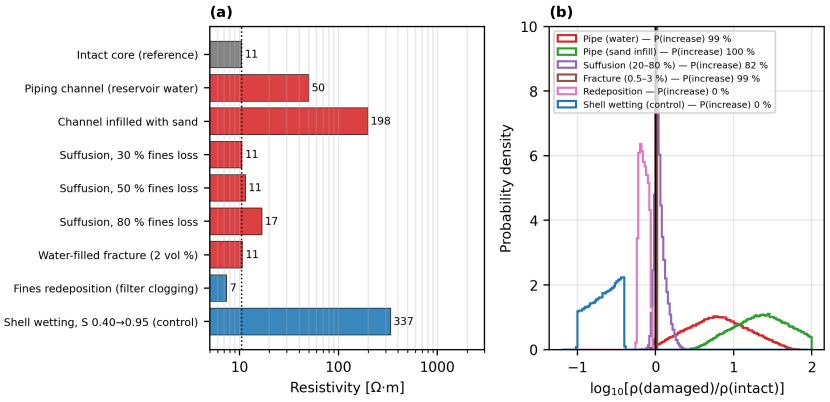

Figure 3: (a) Resistivity of damage end-members for the base case ($\sigma_w = 200\ \mu\mathrm{S\,cm^{-1}}$, intact core 10.5 $\Omega \cdot$ m, dotted line); red bars increase resistivity, blue bars decrease it. The two conductive members are fines redeposition and the downstream-shell wetting control. (b) Monte-Carlo distributions ($N = 2 \times 10^5$) of the damaged-to-intact resistivity ratio with parameter ranges of Section 2.1; P(increase) annotated per scenario.

3.2. Signal scaling and the detection asymmetry

Figure 4 collapses the pipe-defect sweep (diameters 0.5–3 m, depths 5–12 m) onto a single empirical law:

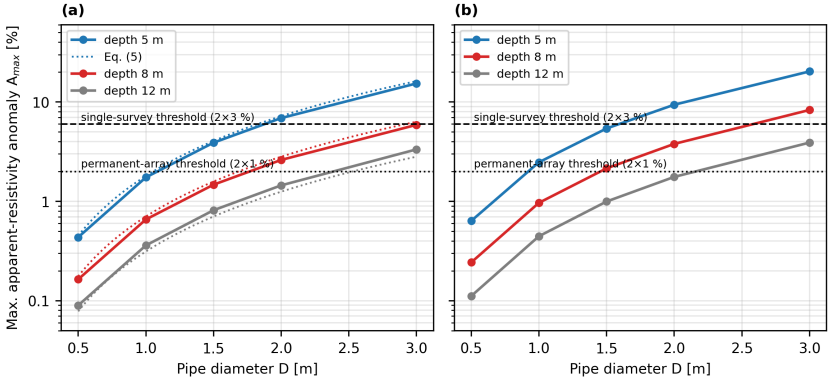

Figure 4: Maximum apparent-resistivity anomaly of a through-going core pipe in a dipole–dipole crest survey (48 electrodes, 2 m spacing) versus pipe diameter, for centre depths of 5, 8 and 12 m. (a) Actual resistive defect (50 $\Omega \cdot$ m in a 10 $\Omega \cdot$ m core); dotted line: the empirical fit $A_{\max} \approx 45(D/z)^2$ (± 25 %). (b) Hypothetical conductive twin of equal contrast magnitude (2 $\Omega \cdot$ m). Horizontal lines: nominal single-survey (2×3 %) and permanent-array (2×1 %) detection thresholds.

$$A_{\max}\,[\%] \approx 45\,(D/z)^2, \qquad \pm 25\,\% \tag{5}$$

where $A_{\max}$ is the largest apparent-resistivity perturbation in a dipole–dipole crest survey. The coefficient 45 embeds the water-filled-pipe contrast of the base case; $A_{\max}$ scales with the logarithmic resistivity contrast as well as with geometry, so a sand-filled or strongly suffused defect of the same diameter plots above this line and a weakly suffused one below it. Refitting the same sweep at 1-, 2- and 4-m electrode spacing returns coefficients of 42–43, and holding the survey fixed while rescaling the embankment returns 40–47 across dam heights of 10–40 m, indicating that Eq. (5) reflects the target-in-dam geometry — and transfers across the practical range of dam sizes — rather than the acquisition layout or the 15-m base case. The law's consequences are immediate. Against the textbook single-survey threshold of twice a 3 % noise floor, detection requires $D/z \gtrsim 0.37$ — a 3-m pipe at 8 m depth, i.e. a defect approaching breach dimensions. Against a permanent-array repeatability of 1 %, $D/z \gtrsim 0.21$. A 1.5-m pipe at 8 m produces 1.47 % (the law of Eq. (5) returns $45 \cdot (1.5/8)^2$

= 1.58 %, the two agreeing inside its ±25 % band): half the noise floor, and the smoothness-constrained inversion of such data is indistinguishable from the defect-free inversion (Fig. 5) — the difference image fluctuates by ±0.4 decades regardless of whether a defect is present, so even a careful comparison of two independently acquired surveys cannot isolate it.

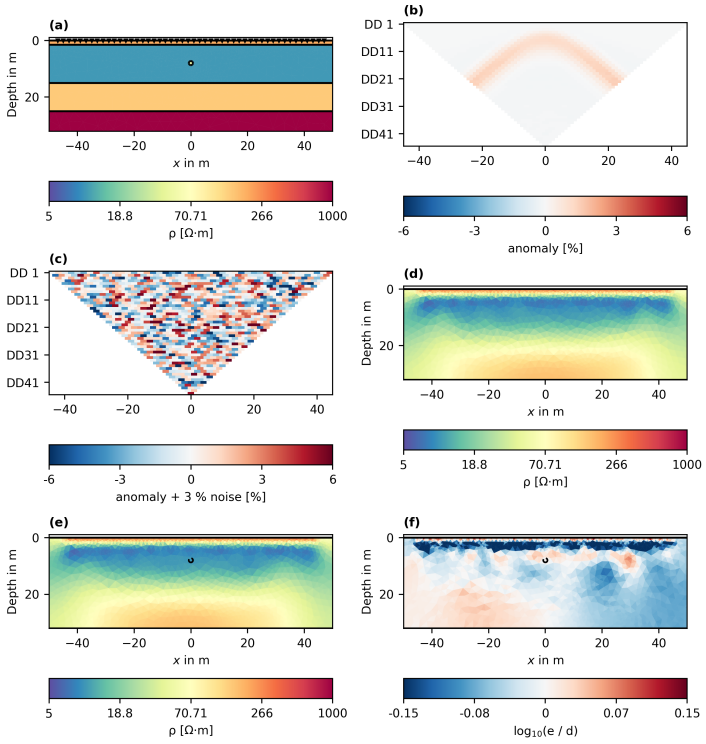

Figure 5: A 1.5-m freshwater pipe (50 Ω · m) at 8 m depth. (a) True model; (b) noise-free data-space anomaly (max 1.5 %); (c) the same signal with 3 % field noise; (d) smoothness-constrained inversion of defect-free data; (e) inversion of the defect data; (f) difference of (e) and (d), fluctuating by ±0.4 decades (dashed circle: true defect position).

The same geometry with the polarity reversed (the conductive target that conventional interpretation *assumes*) is somewhat more visible. In the data space, a 2 Ω · m pipe of equal contrast magnitude yields a signal 1.3–1.5× larger (1.46× for the reference geometry, 1.2–1.5 across the sweep), a deterministic, regularization-free result. The model-space recovery must be read statistically:

averaged over five noise realizations, smoothness inversion recovers 11.0 ± 0.4 % of the resistive and 15.7 ± 0.3 % of the conductive log-contrast for a larger 3-m pipe (two recovery cells), a contrast-recovery-ratio (CRR) asymmetry of ≈1.4, whereas for a sub-threshold 1.5-m pipe the single-cell recovery is dominated by the noise realization (3.1 ± 0.4 % versus 3.6 ± 0.4 %, ratio spanning 0.9–1.9) and supports no reliable asymmetry. Zone-type targets, spanning many cells, recover stably and far better (CRR 0.21–0.30; a 14 $\Omega \cdot$ m degraded panel is imaged at 15.0 $\Omega \cdot$ m). The asymmetry has a simple physical root — current channels around a resistive inclusion but is focused by a conductive one — and a modest but consistent corollary: conductive targets are somewhat more visible in the data and somewhat better recovered by smoothness-constrained inversion, a bias that, accumulated across many published case histories, could tilt the record toward conductive anomalies.

Zone-type degradation restores detectability at realistic scales. A panel of partially suffused core (14 $\Omega \cdot$ m, ×1.4) confined below 6 m depth produces 3.3/7.4/11.8 % for along-dam extents of 2/5/10 m: the 10-m zone clears the single-survey threshold and the 5-m zone the monitoring threshold. The realistic target of a crest survey is therefore not "the pipe" but "the reach of degraded core" — and Section~3.5 quantifies which acquisition mode sees which.

3.3. What else is in the data: confounders at the 10 % scale

A full 3-D model of the dam (reservoir wedge, slopes; 9.0×10^4 prism cells) puts the defect signal in context (Fig. 6). Lowering the reservoir from EL.12 to EL.7 changes crest-line apparent resistivities by up to 13.9 %; the seasonal change of reservoir-water conductivity (+30 % in winter) imprints 13.2 % even with no defect at all; the finite-length 1.5-m pipe itself contributes 2.0 %. The finite-3-D pipe signal exceeds its 2.5-D idealization of 1.47 % by a factor of 1.2–1.4 across all shell-property combinations tested (wet, dry and conductive shell variants): the conductive core acts as a wave-guide between resistive shells, concentrating crest-injected current onto the defect, so the 2.5-D screening law of Eq. 5 is conservative regardless of shell condition. Inverting these 3-D data

with the standard 2-D assumption leaves $\chi^2 = 300$–438 of systematic misfit that the regularized inversion converts into plausible-looking but fictitious structure; sections computed with and without the pipe are visually identical, while the same section recomputed at the lower reservoir level changes conspicuously. A single-epoch crest section is primarily an image of geometry and hydrology, then geology, with the defect last.

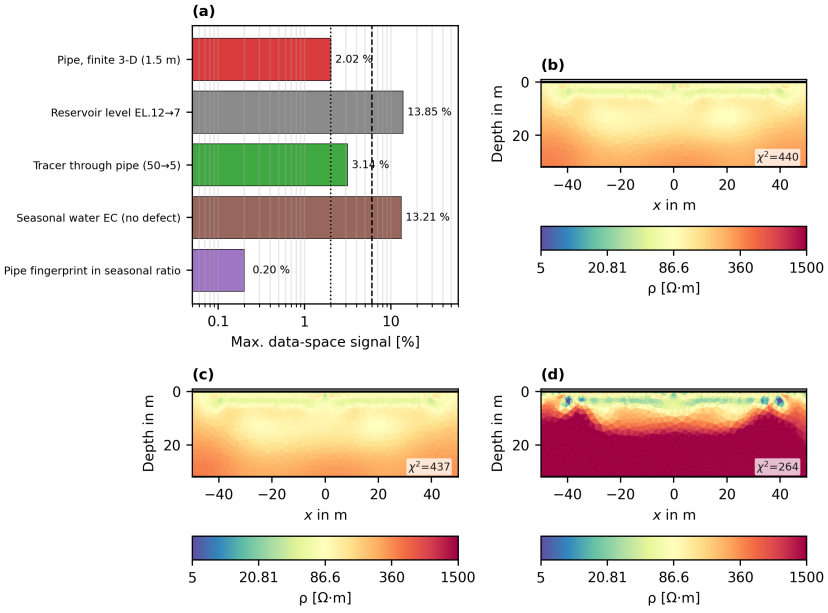

Figure 6: Confounders in full 3-D (reservoir wedge, slopes; $9{\times}10^4$ cells). (a) Crest-line data-space signals: reservoir drawdown 13.9 %, seasonal water-conductivity change 13.2 %, finite-3-D pipe 2.0 %, salt-tracer slug through the same pipe 3.1 %, and pipe fingerprint in a seasonal ratio image 0.2 %. (b)–(d) Standard 2-D inversions of the 3-D data (χ^2 annotated): defect-free (b), defect (c), and the section at the lower reservoir level (d).

3.4. Geological heterogeneity sets the real single-survey threshold

The 6 % threshold of Section~3.2 assumes the only obstacle is instrument noise. Embedding the dam in log-normal heterogeneity ($\sigma_{\ln\rho} = 0.2$–0.35, correlation lengths 5–15 m — the upper value matching the "layered, differentially wetted" core structures actually imaged at Älvkarleby) shows two things (Fig.

7). First, the *paired* (time-lapse) defect signal is essentially invariant: the 3-m pipe's 5.32 % becomes 5.1–5.3 ± 0.3–0.9 %, the 10-m zone's 11.07 % becomes 11.1–11.2 ± 0.4–1.2 % across realizations — differencing on a fixed array cancels the static background almost perfectly. Second, the *unpaired* scatter between realizations — the "geological noise" an interpreter faces when comparing one measured section against an assumed layered reference — has a median of 13.9–25.6 % per datum. The effective single-survey anomaly threshold is therefore not 6 % but $2\sqrt{(3\%)^2 + e_{\mathrm{geo}}^2} = 28$–$52$ %, and in all defect-free realizations tested (N = 20 per heterogeneity combination) the standard criterion (instrument noise only) declares at least one "detectable" anomaly. Single-survey anomaly hunting on an embankment therefore not only misses real defects; it can manufacture spurious ones.

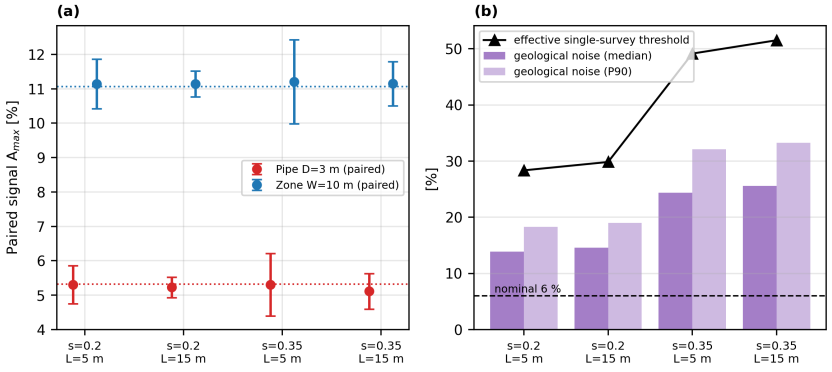

Figure 7: Effect of geostatistical background heterogeneity (log-normal, $\sigma_{\ln \rho} = s$, correlation length L; N = 20 realizations per combination). (a) Paired (time-lapse) defect signal for a 3-m pipe and a 10-m zone: means ±1 s.d. against the homogeneous values (dotted lines). (b) Unpaired realization-to-realization scatter of ρ_a ("geological noise", median and P90 bars) and the resulting effective single-survey anomaly threshold (triangles, $2\sqrt{(3\%)^2 + e_{\mathrm{geo}}^2} = 28$–$52$ %); nominal 6 % threshold dashed.

3.5. What works: mode-dependent minimum detectable defects

Before ranking modes, an apparent contradiction must be resolved. The seasonal change in reservoir-water conductivity appeared in Section~3.3 among

the confounders that overwhelm a single survey, imprinting up to 13 % on the crest apparent resistivities of an *intact* dam; yet that same seasonal contrast is what a time-lapse survey exploits, because a water-connected defect modulates with the reservoir while the surface-conduction-dominated core does not. The seasonal signal is thus noise for a single survey and signal for a monitored one — provided its basin-scale part can be separated from the local defect modulation. It can: forward-modelling the seasonal response of the defect-free dam from its measured covariates (reservoir level, water EC, temperature) and subtracting it from the measured seasonal difference — a model-based background removal expressed here as a double difference — removes, for a 10-m degraded reach in full 3-D, an 8.5 % basin response and leaves a 2.9 % fingerprint localized at the reach (Supplementary Fig. S2), detected with the gradient array at DI = 3.7 (53 qualifying data). Sized so that its single-survey static contrast matches the 2.5-D reach of Table 3 (13.5 % against 11 %), the 3-D monitoring index meets or exceeds its 2.5-D value, so the rankings below are if anything conservative; the identical procedure on a 1.5-m pipe leaves only 0.2 %, below any monitoring floor. The reservoir's own seasonal cycle is therefore a natural contrast agent that recovers reach-type degradation with nothing added to the reservoir — though still not pipes.

Table 3 assembles the framework's prescriptive output, charted in Fig. 8: the detection index for each target × acquisition mode under the voltage-aware error model, using the best standard array per case. The conventional dipole–dipole consistently underperforms because its largest anomalies ride on its lowest-voltage data (Supplementary Fig. S1); a 1-m electrode spacing even *reduces* DI from 0.16 to 0.07 while nominally tripling the signal, and a culled, multi-spacing field-style dipole–dipole set (a = 2/4/6 m, n $\leq$ 6) narrows but does not close the gap (DI 2.1 with only two qualifying data versus 3.2 with twenty-eight for the gradient set on the 10-m zone). The gradient advantage moreover grows with target depth, from parity at 8 m to an order of magnitude at 28 m, although below ~10 m no surface array reaches the threshold for pipe-class targets. In a single survey, no pipe up to 3 m diameter is detectable (DI $\leq$ 1.6);

a 10-m degraded zone is detectable (DI = 3.2; confirmed in full 3-D, where the same target yields DI = 3.3 with 36 qualifying data and a 3-D/2.5-D signal ratio of 0.92–1.00 — zone-type targets gain no wave-guide boost but lose nothing either), and a 5-m zone is marginal (1.9–2.1). Standard-precision monitoring (1 % repeatability) detects nothing the single survey misses; *precision* monitoring (0.5 %, buried electrodes, temperature-corrected, seasonally differenced) brings the 10-m zone to DI = 2.2 and the 5-m zone to the threshold — but leaves even a 3-m pipe at DI = 0.4, because a pipe's seasonal modulation is diluted by its tiny volume. The only surface technique that reaches pipe-class defects is active contrast manipulation: a salt-tracer slug raising reservoir EC $\times 50$ drives the 1.5-m pipe to DI = 2.7–3.7 in same-day differencing (with the bonus of travel-time information), and a $\times 10$ slug suffices for the 5-m zone (DI = 17). A 1.0-m pipe at 8 m depth remains beyond every surface mode considered — an honest floor to the method. Site calibration closes the decision loop: with the reciprocal-fitted error model, predicted DI tracks the true value within ± 13 %, whereas adopting the textbook 3 %/100 μV at face value misjudges detectability by up to $\times 3.2$ (capability wasted on quiet sites, false promises on noisy ones). The pipe non-detections sit far below threshold and hold regardless of the error-model and heterogeneity priors; the marginal cases (the 5-m zone and the gradient-over-dipole–dipole margins) sit close enough to DI = 2 to cross it under modest changes in those priors, and are graded marginal rather than detected for that reason.

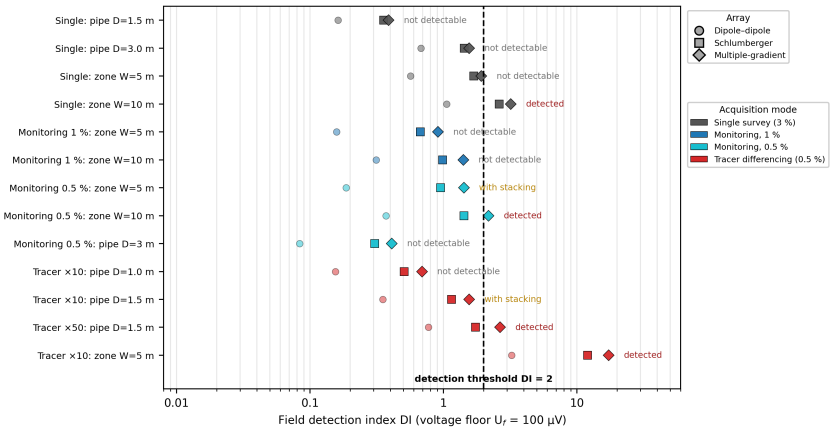

Figure 8: Field detection index (DI, voltage-aware error model, U_f = 100 μV, I = 0.5 A) for each target × acquisition mode; marker shape denotes the array and colour the acquisition mode (legends). Verdicts (right) use the best array; "with stacking" denotes detection only at the U_f = 20 μV noise floor.

Table 3. Field detection index DI per target and acquisition mode (best standard array; values for voltage floors of 100/20 μV). Verdict: Y detected (DI > 2, ≥5 data), S detectable with stacking (20 μV), N not detectable.

Mode	Target	Best array	DI (100 μV)	DI (20 μV)	Verdict
Single survey (p = 3 %)	Pipe D = 1.5 m	GR	0.39	0.43	N
	Pipe D = 3.0 m	GR	1.56	1.73	N
	Zone W = 5 m	GR	1.92	2.13	S
	Zone W = 10 m	GR	3.19	3.58	Y (DD: 1.06 N)
Monitoring, 1 %	Zone W = 5 m	GR	0.91	1.18	N

Mode	Target	Best array	DI (100 μV)	DI (20 μV)	Verdict
	Zone W = 10 m	GR	1.41	1.84	N
Monitoring, 0.5 %	Zone W = 5 m	GR	1.42	2.19	S
	Zone W = 10 m	GR	2.18	3.42	Y
	Pipe D = 3.0 m	GR	0.41	0.64	N
Tracer ×10 (0.5 %)	Pipe D = 1.0 m	GR	0.69	1.08	N
	Pipe D = 1.5 m	GR	1.56	2.44	S
Tracer ×50 (0.5 %)	Pipe D = 1.5 m	GR	2.66	3.73	Y
Tracer ×10 (0.5 %)	Zone W = 5 m	GR	17.3	26.6	Y

3.6. Full-scale benchmark: the Älvkarleby test dam

The framework's end-to-end test is the Älvkarleby experiment, whose published inputs (geometry, laboratory resistivities, defect inventory, electrode layout, reciprocal error level) fully specify our model and whose outcomes were established independently by a monitoring team blind to the defect positions. The site's own measured properties place it deep in the resistive-damage regime of Fig. 2 (core 21 $\Omega \cdot$ m against 240 $\Omega \cdot$ m river water) and the field outcome agrees: every detected engineered defect, the filter defect that emerged after two

years, and the unintended erosion zones confirmed at dismantling all appeared as high-resistivity (and low-chargeability) anomalies (Norooz, 2025; Norooz and Dahlin, 2025). Our forward predictions reproduce the polarity for 6 of 6 defects (one all-resistive prediction, unrefuted across the six, rather than six independent successes). The predicted detection ranking matches the reported difficulty ordering (Table 4 and Fig. 9, long-term-average error scenario: concrete block 5.9 > horizontal sand layer 2.2 ≈ wooden block 2.2 > vertical loose zone 1.4 > end sand layer 0.8 > filter defect 0.3), including the three structural features of the field campaign: nothing was detectable in single-epoch data (all DI < 2 at 1 % error; the field success relied on multi-year daily averaging); the defect nearest the abutment remained blind (coverage, not contrast); and the wooden block's borderline DI is consistent with its becoming visible only after three years, as erosion enlarged its electrical footprint. The concrete block (D4) carries the highest multi-year-average DI (5.9) yet gave only a weak field indication; this is not a discordance but the ≥5-datum rule operating as intended: its anomaly clears the threshold on fewer than five qualifying data (Table 4, note †), so it is correctly graded marginal rather than strongly detected. The single genuine discordance is the vertical loose zone, detected in the field but predicted marginal (DI 1.4), attributable to the field campaign's six horizontal and four near-vertical electrode lines and their crossline measurements, which our reconstruction simplifies. We emphasize what this benchmark is and is not: it supports the polarity physics and the relative detectability calculus on a 4-m-scale structure, but it samples a single point of the (σ_w, CEC) plane deep in the resistive regime, a one-sided test that anchors the resistive arm of the criterion while the conductive arm is exercised separately at HyeonNam (Section~4.1). Because its electrodes are buried in-dam, it fixes the scale-free polarity physics but never engages the crest-injection, resistive-shell geometry on which the full-scale detection limits depend. Extrapolation to 15–50-m dams surveyed from the crest accordingly rests on the scaling analysis of Section~3.2–3.4, which the benchmark's $(D/z)^2$ ordering supports but does not independently prove at full scale. The contribution is accordingly a predictive framework — falsifiable pre-

dictions of polarity, detection limit, and difficulty ranking — checked against the one available controlled full-scale benchmark and a defined retrospective field programme (Section~4.3 step 5), not a field-campaign report.

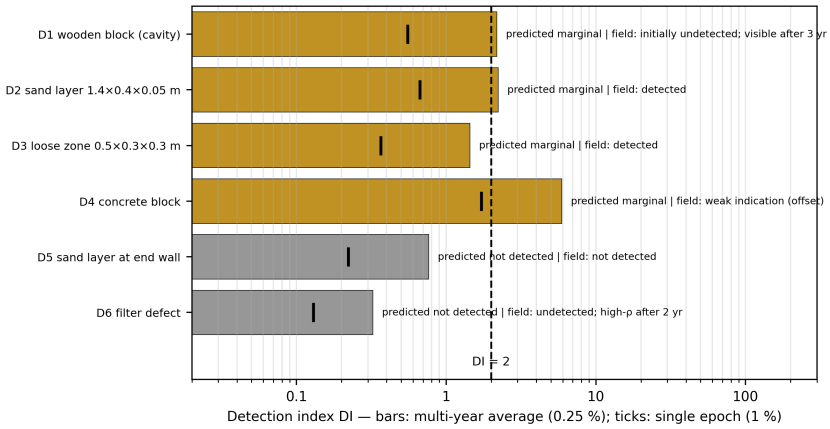

Figure 9: Benchmark against the Älvkarleby full-scale test embankment (model inputs exclusively from published values; field outcomes from [20]). Bars: predicted DI for the multi-year-average error scenario (0.25 %); ticks: single-epoch scenario (1 %); dashed line: detection threshold. Predicted anomaly polarity is resistive for all six defects; per-defect predicted verdict and reported field outcome are annotated.

Table 4. Älvkarleby benchmark: predictions from published inputs versus reported field outcomes (Norooz et al., 2024). DI given for single-epoch (1 %) and multi-year-average (0.25 %) error scenarios; predicted polarity is resistive for all defects, as observed.

Defect (size, m)	DI single	DI averaged	Predicted	Field outcome
D4 concrete block (0.4×0.3×0.2)	1.72	5.91	marginal†	weak indication (positional offset)

Defect (size, m)	DI single	DI averaged	Predicted	Field outcome
D2 sand layer (1.4×0.4×0.05)	0.67	2.23	marginal–detected	detected
D1 wooden block (0.4×0.3×0.15)	0.55	2.18	marginal	undetected; visible after 3 yr
D3 loose zone (0.5×0.3×0.3)	0.37	1.44	marginal (low)	detected
D5 sand layer at end wall (1.3×0.4×0.05)	0.22	0.77	not detected	not detected
D6 filter defect (0.3×0.3×0.15)	0.13	0.32	not detected	undetected; high-ρ zone after 2 yr

† D4: DI exceeds the threshold but with fewer than five qualifying data; polarity and relative detectability are consistent with the weak field indication.

4. Discussion

4.1. One diagram, one literature: reading past and future surveys off the phase plane

The value of Fig. 2 is that it converts a two-decade argument conducted by case history into a coordinate lookup. The Scandinavian experience — Hällby's reliance on seasonal-variation amplitude rather than absolute resistivity (Sjödahl et al., 2008), and Älvkarleby's uniformly high-resistivity defect and erosion signatures — belongs to impoundments at a few tens to a few hundred $\mu\mathrm{S\,cm^{-1}}$, far inside the resistive-damage regime; so do the laboratory suffusion

experiments (Masi et al., 2020), and so does the Korean inland stock at 100–400 μS cm^{-1}. The conventional rule's genuine successes — estuarine barriers, mine-water and tailings facilities, wastewater lagoons — cluster above the crossover, where pore water out-conducts the soil skeleton and a leak really is a conductor. Between the regimes sit instructive boundary cases. At the HyeonNam monitoring dam — instrumented with the modified water-coupled arrays of Lee and Oh (2018) — the measured configuration (reservoir $\approx$500 μS cm^{-1} against a weathered, low-CEC core of 45–80 $\Omega \cdot$ m) makes the conductive-leak assumption self-consistent, and the criterion *endorses* the conventional reading there; yet the same assumption transplanted to a neighbouring reservoir at 200 μS cm^{-1} would silently fail. Regime membership must be computed per dam, from two measurable numbers, not inherited by habit.

Our own retrospective cases illustrate the diagram's second axis of order: location within one dam. The confirmed leakage paths of Lee et al. (2020) — a right-abutment contact and a toe-drain outlet — appeared as low-resistivity anomalies in a ~500 $\Omega \cdot$ m downstream shell, exactly as the criterion predicts for water invading a *granular, surface-conduction-poor* host; and that same paper, citing Oh and Sun (2008), had already cautioned in words that the *core* could behave oppositely. The present framework supplies the quantitative criterion those scattered, qualitative observations lacked: the resistive damage body in the core, the conductive wetting halo and redeposition zone downstream, and the conductive contact leak at the abutment are not competing observations but the three predicted faces of a single leak. We deliberately present these n = 2 sign-level cases as illustrations rather than statistical validation; the systematic retrospective test — projecting a population of confirmed-damage and confirmed-intact dams onto the phase plane with their as-surveyed water chemistry — is defined, templated, and left to a dedicated study.

4.2. What a negative (or positive) survey actually means

The framework replaces the binary "anomaly / no anomaly" with four mutually exclusive readings of a survey outcome. A blank section over a suspect

dam means either (i) no defect, (ii) a defect below the survey's computable detection limit (for a crest survey, any pipe with $D/z < 0.37$, i.e. nearly every pipe that matters), (iii) a defect of the opposite polarity to the one the interpreter shortlisted, or (iv) a defect whose signal is real but buried beneath the 14–26 % geological and hydrological background. Readings (ii)–(iv) are not exotic: Section~3 shows they are the *default* for early core damage in fresh water. A negative survey without an attached detectability calculation is therefore not evidence of integrity, and — the mirror conclusion — a positive low-resistivity anomaly in the core position of a single-epoch freshwater section is most parsimoniously an artefact or a downstream consequence, because the damage itself almost cannot produce it (P $\approx$ 0 %, Section~3.1).

The same physics explains why the literature took so long to notice. Detection is asymmetric: a conductive target of equal geometric contrast is somewhat more visible in the data ($\approx$1.3–1.5$\times$, a deterministic data-space factor) and, where the contrast clears the above-threshold geometry and recovery is measurable, modestly better recovered by smoothness inversion ($\approx$1.4$\times$), so the case histories that could be confirmed and published may — by hypothesis, not as an effect measured here — have leaned toward conductive ones; meanwhile heterogeneity can make any single-epoch section appear anomalous against instrument-noise-only thresholds (spurious indications in all defect-free realizations tested), and excavation downstream of a real leak always finds wet ground to corroborate them. A literature assembled under these selection rules will converge on "low resistivity = leak" without any individual study being wrong. Breaking the loop requires reporting norms as much as physics: publish negative surveys with their detection limits; state the polarity hypothesis before drilling; log the covariates (level, EC, temperature) that dominate the data; and verify high-resistivity core candidates with the same diligence traditionally reserved for conductive ones.

4.3. A pre-survey protocol

The results condense into a sequence a practitioner can execute with five inputs (reservoir EC, core CEC or plasticity-based estimate, porosity, target hypothesis, array geometry) and one optional measurement (a reciprocal subset for site error calibration, 30–60 min of acquisition):

1. **Locate the dam on the phase plane** (Eq. 1a). This fixes the expected polarity of each damage mode and decides whether the conventional rule applies at all.
2. **Compute the detection limit before contracting the survey** (Eq. 5 + DI with site-calibrated p, U_f). If the credible target is a pipe and the computed minimum detectable diameter exceeds plausible defect sizes, a single survey cannot answer the question being asked — and should either be re-scoped to zone-type targets or replaced by a time-lapse design.
3. **Acquire with the voltage budget in mind**: gradient-type or Schlumberger-type configurations carry the defect signal on measurable voltages; reciprocal measurements quantify the actual error model; reservoir level, water EC and temperature are logged as mandatory covariates.
4. **Escalate along the time axis, not the spacing axis.** Denser electrodes do not pay (Section~3.5); repetition does. The reservoir's own seasonal cycle of conductivity and temperature is a natural contrast agent — a water-connected defect modulates with it, the surface-conduction core does not — so a permanent, buried array differenced across seasons, with the basin-scale response removed by a measured-covariate forward model (Section~3.5), detects ≥5–10-m degraded reaches at 0.5 % repeatability with nothing added to the reservoir; this is the primary monitoring route. Pipe-class defects are too small to modulate detectably even seasonally: the only surface option that reaches them is an active salt-tracer slug (EC ×10–50), which — given the environmental and regulatory limits on salinating a freshwater reservoir — is a conditional, localized- or downstream-injection technique, not a routine one. Pipe-scale early de-

tection is better delegated to complementary channels: induced polarization, whose normalized chargeability falls with clay loss regardless of water chemistry and so resolves the residual ambiguity of pure DC measurements, and point or fibre-optic seepage instrumentation. We model DC resistivity only, so the low-chargeability that accompanied the Älvkarleby high-resistivity anomalies enters here as corroborating field evidence rather than as a modelled quantity, and its quantitative integration is left to future work. A one-page reporting checklist condenses the protocol; we propose it accompany every embankment ERT report: (i) reservoir EC and water temperature at survey time; (ii) reservoir level; (iii) core CEC (or plasticity proxy) and porosity; (iv) assumed damage mode and the polarity it predicts; (v) array, spacing and reciprocal-error parameters (p, U_f); (vi) the estimated minimum detectable defect size from Eq. (5) and the detection index; (vii) whether the interpretation is single-epoch or time-lapse.

5. **Close the loop after verification.** Each drilled or excavated candidate, confirmed or refuted, is one row in the retrospective template; ten rows constitute the field confusion matrix this framework still lacks.

4.4. Limitations

Six boundaries of the present analysis deserve emphasis. First, real pipes evolve: a growing channel carries a wetting and stress-relief halo whose conductive contribution competes with the resistive channel core. The phase diagram brackets the end states, and the Älvkarleby time histories (defects becoming visible over 2–3 years as erosion matured) (Norooz, 2025) suggest evolution *toward* detectability, but coupled seepage–erosion–resistivity modelling (and with it, the time-to-detectability of a monitoring installation) remains future work. Second, our heterogeneity model is statistical; engineered fills carry structured, anisotropic layering whose artefacts may organize differently than the log-normal fields assumed here, although the conclusion they support (difference, don't hunt) is insensitive to that distinction. Third, the error-model

parameters are site variables by construction; the calibration procedure transfers, the default numbers do not, and non-Gaussian interference (powerlines, pumping stations) is flagged by, but not modelled in, the binned-reciprocal diagnostic; and because the array ranking of Section~3.5 rests on a finite voltage floor, it converges toward parity at exceptionally quiet, heavily stacked sites — it is a statement about realistic noise floors, not about array physics in the abstract. Fourth, the benchmark validates the physics at 4-m scale with in-dam electrodes; full-scale validation from the crest is indirect, resting on the scaling law and the 3-D analyses, and is the precise gap the retrospective programme of Section~4.3(5) is designed to close. Fifth, the survey geometry is only partly varied: the Eq. (5) coefficient proves stable across 1–4-m electrode spacing (42–43) and across dam heights of 10–40 m (40–47), and the depth trend is verified to 28 m, so the screening law transfers across dam size; systematic rescaling with crest width and slope angle is the residual geometric dimension left to future work. Sixth, we model DC resistivity only: induced polarization (whose clay-specific normalized chargeability falls with fines loss independently of water chemistry, and which accompanied the Älvkarleby high-resistivity anomalies as a low-chargeability signature (Norooz and Dahlin, 2025)) is the natural complementary channel for resolving the residual polarity ambiguity of pure DC data, and its quantitative integration is left to future work.

5. Conclusions

1. In freshwater embankment dams, ~97 % of intact clay-core conduction is surface conduction; consequently piping and suffusion *raise* resistivity (×1.6–19 when advanced; P = 82–100 %), as repeatedly observed but not previously predicted, and the closed-form criterion $\sigma_w(F^* - 1) > B\,Q_v$ with the (σ_w, CEC) phase diagram tells any given dam which interpretation regime it is in. Typical inland reservoirs lie a factor 3–10 inside the resistive-damage regime.
2. For the reference crest-survey geometry, pipe-defect signals follow $A_{\max} \approx$

$45(D/z)^2$ ($\pm$25 %, verified to 28 m depth); under the voltage-dependent error levels tested here, none of the standard surface arrays reliably detects a $\leq$3-m freshwater pipe in single-epoch data, and geological heterogeneity raises the effective single-survey threshold to 28–52 %, generating spurious anomalies in all defect-free realizations tested. "No anomaly" is therefore not evidence of "no defect", and single-epoch low-resistivity anomalies in the core position are most parsimoniously artefacts or downstream consequences. The detectable signature is not the narrow channel but the reach of degraded core that surrounds and feeds it — the resistive erosion front, its conductive wetting-and-leakage halo, and the seepage consequences downstream — which is what crest ERT should survey for, tracking its growth along the time axis.

3. Conductive targets are modestly but consistently more visible than resistive ones of equal contrast (data-space factor $\approx$1.3–1.5; inversion-recovery factor $\approx$1.4, averaged over noise realizations) — a bias that, accumulated across many case histories, could contribute to the predominance of conductive "successes" in the literature.
4. Minimum detectable damage is quantified per monitoring mode: a single gradient-type survey resolves $\geq$10-m degraded reaches; permanent-array monitoring resolves $\geq$5-m reaches at 0.5 % repeatability using the reservoir's own seasonal conductivity cycle as a natural contrast agent, the basin-scale seasonal response being separable from the local fingerprint by a measured-covariate model (DI = 3.7 for a 10-m reach in full 3-D, nothing added to the reservoir). Pipe-class defects lie below every passive surface mode — a 1.5-m pipe is reached only by an active, non-routine salt-tracer slug and a 1-m pipe by none — so pipe-scale early detection is delegated to complementary channels (induced polarization, seepage instrumentation). Reciprocal-based site calibration ties each verdict to the site's measured error model (true detectability recovered to $\pm$13 % in silico); field falsification is the retrospective programme of Section~4.3.
5. A reconstruction of the Älvkarleby full-scale experiment from published

inputs alone reproduces the anomaly polarity (a single all-resistive prediction, unrefuted across six defects), the detection ranking, the abutment blind spot, and the necessity of multi-year averaging — an out-of-sample consistency check on a controlled full-scale test embankment.

6. All scripts and result files reproducing every figure and table are openly archived on Zenodo (DOI: https://doi.org/10.5281/zenodo.20658789); the pre-survey detectability assessment runs from five inputs (reservoir EC, core CEC/porosity, target hypothesis, array, site error parameters).

CRediT authorship contribution statement

Seokhoon Oh: Conceptualization, Methodology, Software, Validation, Formal analysis, Resources, Data curation, Writing – original draft, Writing – review & editing, Visualization, Supervision, Project administration, Funding acquisition.

Declaration of competing interest

The author declares that he has no known competing financial interests or personal relationships that could have appeared to influence the work reported in this paper.

Acknowledgements

This research was supported by the Basic Science Research Program through the National Research Foundation of Korea (NRF), funded by the Ministry of Education (RS-2019-NR040076); by the Institute for Korea Spent Nuclear Fuel (iKSNF) and the Korea Foundation of Nuclear Safety (KoFONS) grant funded by the Korean government (Nuclear Safety and Security Commission, NSSC) (RS-2021-KN066110); and by the NRF grant funded by the Korean government (Ministry of Science and ICT, MSIT) (No. 2022R1A2C1092301). The funding sources had no involvement in the study design; in the collection, analysis and

interpretation of data; in the writing of the report; or in the decision to submit the article for publication.

Data and code availability

All scripts and result files required to reproduce every figure and table are openly available on Zenodo (Oh, 2026; https://doi.org/10.5281/zenodo.20658789). The Älvkarleby benchmark uses only published values as model input.

Supplementary material

Supplementary Fig. S1 (the voltage-allocation mechanism underlying array performance: measured voltage versus anomaly magnitude over the same defect, for (a) the dipole–dipole and (b) the multiple-gradient set) and Supplementary Fig. S2 (separability of the seasonal confounder in full 3-D: (a) the data-space magnitudes of the measured seasonal difference with the degraded reach present, the intact-dam basin model, and their double difference, relative to the monitoring floor; (b) the double-difference residual in section, localized at the degraded reach) accompany this article.

Declaration of generative AI and AI-assisted technologies in the writing process

During the preparation of this manuscript, generative AI tools were used to assist with language editing. All analyses and results were designed, validated, and verified by the author.

References

Archie, G.E., 1942. The electrical resistivity log as an aid in determining some reservoir characteristics. Transactions of the AIME 146, 54–62. https://doi.org/10.2118/942054-G

Cho, I.K., Yeom, J.Y., 2007. Crossline resistivity tomography for the delineation of anomalous seepage pathways in an embankment dam. Geophysics 72 (2), G31–G38. https://doi.org/10.1190/1.2435200

Dahlin, T., Zhou, B., 2004. A numerical comparison of 2D resistivity imaging with 10 electrode arrays. Geophysical Prospecting 52, 379–398. https://doi.org/10.1111/j.1365-2478.2004.00423.x

LaBrecque, D.J., Yang, X., 2001. Difference inversion of ERT data: a fast inversion method for 3-D in situ monitoring. Journal of Environmental and Engineering Geophysics 6 (2), 83–89. https://doi.org/10.4133/JEEG6.2.83

Lee, B., Oh, S., 2018. Modified electrical survey for effective leakage detection at concrete hydraulic facilities. Journal of Applied Geophysics 149, 114–130. https://doi.org/10.1016/j.jappgeo.2017.08.006

Lee, B., Oh, S., Yi, M.-J., 2020. Mapping of leakage paths in damaged embankment using modified resistivity array method. Engineering Geology 266, 105469. https://doi.org/10.1016/j.enggeo.2019.105469

Masi, M., Ferdos, F., Losito, G., Solari, L., 2020. Monitoring of internal erosion processes by time-lapse electrical resistivity tomography. Journal of Hydrology 589, 125340. https://doi.org/10.1016/j.jhydrol.2020.125340

Norooz, R., 2025. Monitoring techniques for embankment dams: a study on ERT and IP measurements, and seepage modelling of the Älvkarleby test dam. Doctoral thesis, Lund University, Lund, Sweden. ISBN 978-91-8104-671-7. https://lup.lub.lu.se/record/2092bc1a-c1ea-4c35-aeda-8417404fe352

Norooz, R., Dahlin, T., 2025. 3D DCIP techniques for detection of internal defects in the Älvkarleby test dam. In: NSG 2025: 4th Conference on Geophysics for Infrastructure Planning, Monitoring and BIM. European Association of Geoscientists & Engineers, pp. 1–5. https://doi.org/10.3997/2214-4609.202520114

Norooz, R., Olsson, P.-I., Dahlin, T., Günther, T., Bernstone, C., 2021. A geoelectrical pre-study of Älvkarleby test embankment dam: 3D forward modelling and effects of structural constraints on the 3D inversion model of zoned embankment dams. Journal of Applied Geophysics 191, 104355. https://doi.org/10.1016/j.jappgeo.2021.104355

Norooz, R., Nivorlis, A., Olsson, P.-I., Günther, T., Bernstone, C., Dahlin, T., 2024. Monitoring of Älvkarleby test embankment dam using 3D electrical resistivity tomography for detection of internal defects. Journal of Civil Structural Health Monitoring 14, 1275–1294. https://doi.org/10.1007/s13349-024-00785-x

Oh, S., 2012. Electrical resistivity response due to variation in embankment shape and reservoir levels. Environmental Earth Sciences 65, 571–579. https://doi.org/10.1007/s12665-011-1104-y

Oh, S., 2026. Reproduction package — A petrophysical framework for internal-erosion monitoring of freshwater embankment dams: anomaly polarity, detection limits, and a full-scale benchmark (v1.0). Zenodo. https://doi.org/10.5281/zenodo.20658789

Oh, S., Sun, C.-G., 2008. Combined analysis of electrical resistivity and geotechnical SPT blow counts for the safety assessment of fill dam. Environmental Geology 54 (1), 31–42. https://doi.org/10.1007/s00254-007-0790-y

Rücker, C., Günther, T., Wagner, F.M., 2017. pyGIMLi: an open-source library for modelling and inversion in geophysics. Computers & Geosciences 109, 106–123. https://doi.org/10.1016/j.cageo.2017.07.011

Sjödahl, P., Dahlin, T., Zhou, B., 2006. 2.5D resistivity modeling of embankment dams to assess influence from geometry and material properties. Geophysics 71 (3), G107–G114. https://doi.org/10.1190/1.2198217

Sjödahl, P., Dahlin, T., Johansson, S., 2008. Resistivity monitoring for leakage and internal erosion detection at Hällby embankment dam. Journal of Applied Geophysics 65 (3–4), 155–164. https://doi.org/10.1016/j.jappgeo.2008.07.003

Stummer, P., Maurer, H., Green, A.G., 2004. Experimental design: electrical resistivity data sets that provide optimum subsurface information. Geophysics 69, 120–139. https://doi.org/10.1190/1.1649381

Tso, C.-H.M., Kuras, O., Wilkinson, P.B., Uhlemann, S., Chambers, J.E., Meldrum, P.I., Graham, J., Sherlock, E.F., Binley, A., 2017. Improved characterisation and modelling of measurement errors in electrical resistivity tomography (ERT) surveys. Journal of Applied Geophysics 146, 103–119. https://doi.org/10.1016/j.jappgeo.2017.09.009

Waxman, M.H., Smits, L.J.M., 1968. Electrical conductivities in oil-bearing shaly sands. Society of Petroleum Engineers Journal 8 (2), 107–122. https://doi.org/10.2118/1863-A

Wilkinson, P.B., Meldrum, P.I., Chambers, J.E., Kuras, O., Ogilvy, R.D., 2006. Improved strategies for the automatic selection of optimized sets of electrical resistivity tomography measurement configurations. Geophysical Journal International 167, 1119–1126. https://doi.org/10.1111/j.1365-246X.2006.03196.x

Wilkinson, P.B., Loke, M.H., Meldrum, P.I., Chambers, J.E., Kuras, O., Gunn, D.A.,

Ogilvy, R.D., 2012. Practical aspects of applied optimized survey design for electrical resistivity tomography. Geophysical Journal International 189, 428–440. https://doi.org/10.1111/j.1365-246X.2012.05372.x